JGR Space Physics

RESEARCH ARTICLE
10.1029/2020JA028915

Key Points:

- Three low-density cells, including two in the dawn sector and one in the night sector were observed by Gravity Recovery and Climate Experiment at 350 km
- The critical height of low-density cells is shown to be not less than 350 km, which is not consistent with the theoretical prediction
- The effect of vertical winds can be comparable with that of horizontal winds when energetic particles are injected into the auroral region

Correspondence to:
S. Jin,
sgjin@shao.ac.cn

Citation:
Yuan, L., & Jin, S. (2021). Observational evidence and formation mechanism of low-density cells in the upper thermosphere on September 8, 2017. *Journal of Geophysical Research: Space Physics*, *126*, e2020JA028915. https://doi.org/10.1029/2020JA028915

Received 12 NOV 2020
Accepted 17 DEC 2020

Observational Evidence and Formation Mechanism of Low-Density Cells in the Upper Thermosphere on September 8, 2017

Liangliang Yuan[1,2,3], **and Shuanggen Jin**[1,2,4]

[1]Shanghai Astronomical Observatory, Chinese Academy of Sciences, Shanghai, China, [2]University of Chinese Academy of Sciences, Beijing, China, [3]Institute of Solar-Terrestrial Physics, German Aerospace Center, Neustrelitz, Germany, [4]School of Remote Sensing and Geomatics Engineering, Nanjing University of Information Science and Technology, Nanjing, China

Abstract The low-density cell structure in the high-latitude thermosphere is referred to as the density depletion with respect to the adjacent area. Based on Gravity Recovery and Climate Experiment (GRACE) accelerometer data during the September 2017 geomagnetic storms, the thermospheric mass density at about 350 km are estimated and further investigated especially in the high-latitude regions. At least two kinds of low-density cells over the Southern Hemisphere (SH) are observed along the GRACE orbit. To understand the low-density cell structures over the SH observed by GRACE, we investigate the underlying physical mechanism based on thermosphere-ionosphere numerical simulations using Thermosphere-Ionosphere Electrodynamic General Circulation Model and Global Ionosphere Thermosphere Model. According to the simulation results, the formation mechanism of the low-density cell is attributed to the storm-time vertical advection and horizontal velocity divergence driven by the auroral ion convection. The critical height of observable low-density cells is shown to be not less than 350 km. The meridional spatial scale of observed low-density cells over the SH are approximately or slightly larger than 1,500 km. Three low-density cells, including two in the dawn sector and one in the night sector were observed about 1 hour after the direction of interplanetary magnetic field B_Y component reversed. The occurrence of thermospheric low-density structure is essential to be included in the empirical model during geomagnetic storm time.

1. Introduction

The Earth's upper atmosphere is a complex coupled system, within which most low-earth orbiters (LEO) are operating. Spatial-temporal variations of thermospheric mass density are not yet well understood in both theoretical and observational perspectives. Thermospheric neutral mass density is mainly affected by the solar heating during the geomagnetic quiet period. The maximal and minimal value of neutral mass density are attained after noon and midnight over equatorial regions. In the recent two decades, the accelerometer and precise orbit determination have been the two major approaches to precisely estimate thermospheric total mass density (Bruinsma et al., 2004; Calabia & Jin, , 2017; Jin et al., 2018; Sutton et al., 2005) and widely employed to investigate thermospheric variations driven by Joules heating and air upwelling during geomagnetic storms (Bruinsma et al., 2006; Forbes et al., 1996; Liu & Lühr, 2005). Thermospheric mass density responses to geomagnetic storms are more likely to be captured in the high-latitude regions where the solar wind can access easily into the upper atmosphere through the Earth's magnetic reconnection. The thermospheric mass density responses to geomagnetic storms in high latitude regions are complex and closely related to the magnetospheric energy input and thermosphere dynamics. The mass density variation at a given altitude can be caused by many processes such as gravity waves, the accumulative effect of scale height profile and other ionosphere-thermosphere coupling processes.

High-latitude thermospheric density cells are known as the region where the neutral mass density is increased or decreased with respect to the adjacent area. Crowley et al. (1989) first predicted the cell structure of neutral density with diameters of about 1,000–2,000 km based on the simulations of National Center for Atmospheric Research Thermosphere General Circulation Model (TGCM). As proposed by Schoendorf and Crowley (1995) and Crowley et al. (1996), the density cell structures should be inherent features of the neutral thermosphere in the high-latitude region. The mechanism of thermospheric low-density cells were

concluded as the typical dynamic meteorology and anomalous antibaric flow due to the high-speed winds (Schoendorf et al., 1996). However, the vertical motion has not been discussed in their research. The horizontal motions of air parcels in auroral regions are dominated by pressure gradients and ion drags while the vertical motions are dominated by the gravity and buoyancy forces. During magnetically disturbed time such as geomagnetic storms, due to the horizontal transportation and induced pressure gradient by ion convection pattern changes, both horizontal and vertical winds may become so large in the high-latitude region that significant large-scale thermospheric circulation is developed. However, all the evidences for the thermospheric density cell structures are focused on the lower thermosphere, and the numerical simulations also showed that the density cells are restricted to be observed below about 350 km, which has not been compared to in situ observations Crowley et al. (1996). Besides, the possible role that vertical winds can play in the formation of thermospheric cell structures is not discussed in their TGCM simulations. As is indicated by Guo et al. (2019), the vertical wind can be one of the dominant drivers of the thermospheric density cell structures. According to the conservation of perturbation energy in the numerical simulations, the magnitude of the vertical wind perturbation increases with the altitude and reaches 150 (250) m/s at 300 (430) km during the disturbance (Deng & Ridley, 2007). Various studies have also reported strong vertical wind observations that reached more than 100 m/s in the thermosphere from Wind and Temperature Spectrometer instruments on Dynamics Explorer 2 (Innis & Conde, 2002) and Fabry-Perot interferometers measurements (Aruliah et al., 2005; Smith & Hernandez, 1995).

In this study, the thermospheric low-density cells are estimated and investigated in the high-latitude regions during the September 2017 geomagnetic storms based on Gravity Recovery and Climate Experiment (GRACE) accelerometer data. In order to further confirm the GRACE in situ observation and interpret the underlying formation mechanism of the low-density cells, two first-principle models, that is, Thermosphere-Ionosphere Electrodynamic General Circulation Model and Global Ionosphere Thermosphere Model, are adopted for investigating the roles of vertical winds during the disturbed period. The possible effect of interplanetary magnetic field (IMF) on thermospheric density cells is also investigated. The consistencies and discrepancies between observations and simulations are also analyzed.

2. Data and Storm-Time Geophysical Condition

The geomagnetic and interplanetary conditions were examined using the three components of the IMF, auroral electrojet index (AE), SYM-H index, plasma speed, proton temperature, and proton density during 6–8 September 2017 in Figure 1. These data can be found at the NASA website https://spdf.gsfc.nasa.gov/. The first geomagnetic storm started with a Storm Sudden Commencement (SSC) started at 2302 UT on 7 September 2017 (Araki, 1994). The main phase started at 2307 UT on 7 September and reaches its maximum phase (SYM-H = −146 nT) at around 0108 UT on 8 September. And the latter storm reached its maximum phase (SYM-H = −115 nT) at around 1356 UT on 8 September. These data were obtained from http://omniweb.gsfc.nasa.gov/. The IMF Bz showed quite remarkable fluctuations on 7 and 8 September, which is supposed to be as a consequence of two SSC at 2343 UT on 6 September and 2302 UT on September 7, 2017 (http://isgi.unistra.fr/). The first SSC caused the northward turning of IMF Bz around 0000 UT on 7 September with a maximal value of ∼18 nT. Subsequently, Bz kept southward for over 11 h (from 0100 UT to 1200 UT) with an average value of ∼ −8 nT. It later had a sharp southward turn at ∼2040 UT and remained so till ∼2330 UT on 7 September and attained its first minimal value of 30 nT at midnight. Then it reached second minimum value of ∼15 nT at ∼1150 UT on 8 September. The AE index increased beyond 500 nT on 7 September between 0300 and 1000 UT. While the AE values as at the times of the first and second IMF Bz minima became suddenly enhanced and reached about ∼2,300 and ∼2,500 nT, respectively. The SYM-H index showed minima values of −146 and −115 nT at ∼0108 UT and ∼1356 UT on September 8, respectively. The solar wind speed increased rapidly from around 500 km/s to 700 km/s at 2302UT on 7 September and attained its maximum with a value of ∼820 km/s. Compared with above indices, IMF B_Y is more fluctuating and frequently turned between positive and negative on 8 September. The detailed effect of IMF B_Y on the thermospheric will be discussed in Section 3.2.

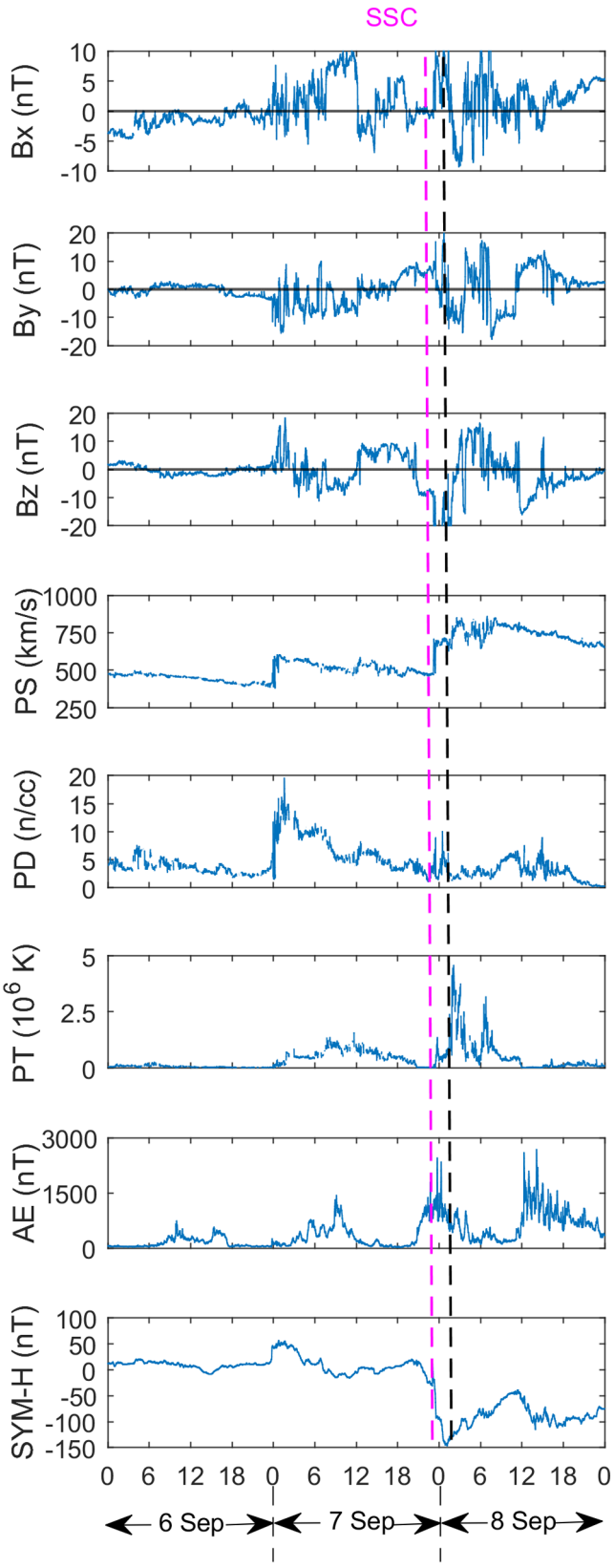

Figure 1. Different indices during 6–8 September 2017 geomagnetic storm events. The purple dashed line represents the storm sudden commencement (SSC) at 2302 UT on September 7, 2017. The black dashed line represents the sudden increases of solar wind plasma temperature and speed that will be discussed in Section 4.

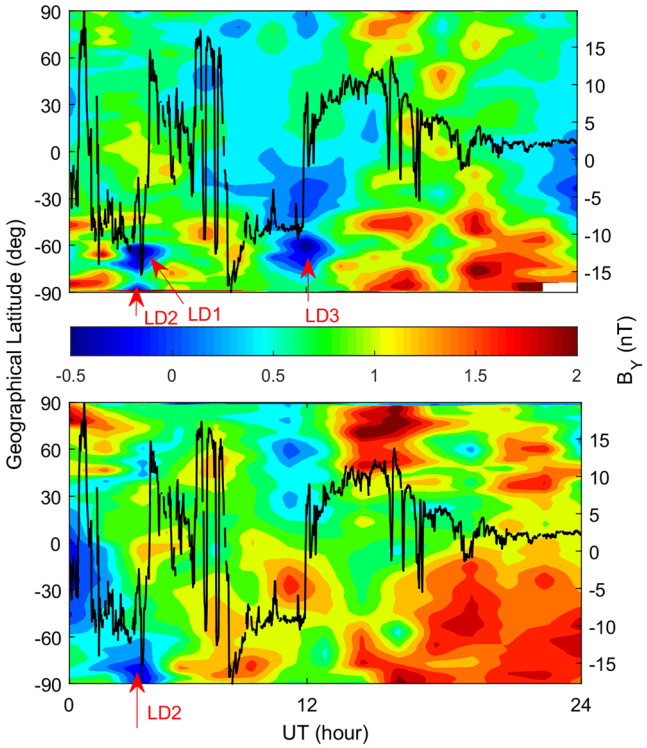

Figure 2. Thermospheric mass density deviations from the reference time values based on GRACE observations on September 8, 2017. Top panel and bottom panel represent day time (~LT 0930) and night time (~LT 2130), respectively. The black solid line represents the IMF B_Y component. GRACE, Gravity Recovery and Climate Experiment; IMF, interplanetary magnetic field.

2.1. Thermospheric Mass Density Observations

In this section, accelerometer-based thermospheric mass density estimates are derived from the Level 1B data of GRACE-A missions, including accelerometer, navigation, thruster, and star-camera measurements. Based on the air drag formula the thermospheric mass density can be estimated by calibrated accelerometer observations onboard LEO satellites.

$$\begin{cases} F_D = \frac{1}{2}\mathrm{CA}\rho v_r^2 \\ v_r = -\dot{r}_{\mathrm{sat}} + v_c + v_w \end{cases} \quad (1)$$

where F_D is the air drag force, C is the drag coefficient, A is the cross-sectional area perpendicular to v_r, ρ is the mass density, v_r is the relative velocity of the atmosphere with respect to the spacecraft, which includes the spacecraft velocity $\dot{r}_{\mathrm{sat}}$, the co-rotating atmosphere velocity v_c and horizontal winds velocity v_w. The detailed processing strategy can be found in Yuan et al. (2019). We also refer to the alternative method proposed by Doornbos et al. (2014).

Mass density percentage deviations from a reference value can be useful in extracting the features of thermosphere neutral mass density cell. The deviations are calculated as follows

$$\rho_{\mathrm{dev}} = \frac{\rho_{\mathrm{storm}} - \rho_{\mathrm{reference}}}{\rho_{\mathrm{quiet}}} \quad (2)$$

where the ρ_{storm} and $\rho_{\mathrm{reference}}$ represent the thermospheric mass density during storm time and reference time, respectively. In order to get rid of the small-scale density disturbances, a 30-sample (~150 s, 1,200 km) running average is taken. This effectively extracts scales of half the length of the window, that is, 600 km. Because of the data gap of GRACE accelerometer, it is not possible to derive the mass density based on in situ measurements in the past few days before 7 September. The values at 0000 UT on 7 September are regarded as the reference value throughout the study if no exception is noted. Figure 2 illustrates the deviations from the reference time values of thermospheric mass density based on GRACE observations. As we can see, three low-density cells were forming in the high-latitude regions successively during the first geomagnetic storm. The first two low-density cells LD1 and LD2 were captured at around 0310 UT and LD3 at around 1120 UT. The latitudinally spatial scales of observed low-density cells over the SH are about 1,500–2,000 km considering that GRACE orbit may not cross the center of the cell. Two low-density cells (LD1 and LD3) in Figure 2 can be classified into the dawn sector low-density cell while the other one (LD2) can be classified into dusk or night sector low-density cell. According to the analyses for the thermosphere at 200 km by Crowley et al. (1996), the total number of low-density cell structures is supposed to dependent on the cross polar cap potential drop and altitudes and can be classified into three scenarios, namely one-, two- and four-cell pattern. At the recovery phase of the first storm, the existence of the low-density cell pair, that is low-density 1 (LD1) and LD2, indicates that a four-cell pattern is probably formed over the SH. However, the existence of the solitary cell LD3 indicates that four-cell pattern disappeared and instead a two-cell or three-cell pattern is likely to be generated over the SH. We note that the three observed low-density cells in the dawn sector and night sector were formed just before IMF B_Y turned from negative to positive. The formation and extinction of low-density cells can probably be related to the reversion of the direction of IMF B_Y component provided the effects of atmospheric waves are excluded. A clockwise rotation of the potential pattern resulting from a change from B_Y-negative to B_Y-positive drives a corresponding rotation in the wind, neutral density, and composition distributions (Crowley et al., 2006). Besides the simulations done by Crowley et al. (2006), the GRACE in situ observation provides another evidence that changes the direction of B_Y can affect the efficiency of the formation of low-density cells. We note that as is concluded by

Yamazaki et al. (2015) the negative (positive) B_Y condition is beneficial for the development of low-density cells over the NH (SH). In later Section, we will further discuss the mass density morphology in comparison with simulations.

2.2. Thermospheric O/N_2

The Global Ultraviolet Imager (GUVI) is one of the four instruments onboard the Thermosphere Ionosphere Mesosphere Energetics and Dynamics (TIMED) satellite, which is the first mission of the NASA Solar Connectivity Program. The TIMED spacecraft is manufactured by the Johns Hopkins University Applied Physics Laboratory. TIMED is designed to study the energy and dynamics of the middle and lower thermal layers between approximately 60 and 180 km range. GUVI can observe the columnar O/N_2 ratio, which is defined as the ratio of the atomic oxygen column density to the nitrogen molecule column density at a height where the nitrogen molecular column density is greater than 10^{17} cm^{-2}. Observations can be determined by the spectral emission lines of oxygen atoms and nitrogen molecules (Meier et al., 2005; Strickland et al., 1995). The orbital inclination of the TIMED satellite is 74.1°. During the geomagnetic storm in September 2017, the local time coverage of TIMED GUVI was around 10:40 LT. Due to the rotation of the earth, TIMED will provide global observations at different longitude and different UT times every day. Therefore, for 1 or a few days, these GUVI observations can be interpreted as global measurements at a relatively fixed LT.

As is known, the general circulation of the Earth's atmosphere may tend to eliminate the horizontal gradient of the Earth's atmospheric scale height. However, during geomagnetic storms the upper atmosphere is likely to deviate far from a steady state. In some cases, the horizontal gradients of atmospheric scale heights are not completely eliminated because of the Coriolis forces, centrifugal forces and the presence of acoustic-gravity waves. The change in the neutral atmospheric density scale height on a fixed altitude surface mainly comes from two factors, namely the change in the isobaric surface height and the atmospheric circulation caused by the vertical wind and changes in atmospheric composition. Moreover, the dominant background atmospheric component at different altitudes is usually the decisive factor. As is known, the density scale heights of different components are inversely proportional to the molecular or atomic mass. As the altitude increases, the dominant component of the atmosphere will gradually tend to have a low molecular mass, due to that the eccentricity of the LEO satellite orbit is not zero, the height of the perigee and apogee will differ by several tens of kilometers or more. Due to the transition height of different components, and the transition height depends on the neutral atmospheric density scale height and atmospheric dynamics such as seasonal factors, geographical location and etc. For example, the transition height of He and O atoms in the summer hemisphere polar region with low solar activity is about 750 km and about 400 km in the winter hemispheric polar region. And therefore, LEO satellite atmospheric density observations around 400 km may be affected by the effect of the asymmetry of the transition height (Thayer et al., 2012). During the September 2017 geomagnetic storm, due to the date of geomagnetic storm approaching the September equinox and the GRACE satellite's orbital height is about 350 km which is lower than 400 km, the effect of the interhemispheric asymmetry of the He/O atomic transition height can be neglected. According to the GUVI observation, as shown in Figure 3, two abrupt changes of the O/N_2 ratio are shown by the solid red line several tens of minutes after the storm onsets. One main feature is that the O/N_2 ratio decreases in the mid- and high-latitude region while increasing in the equatorial region, which is cause by the high-latitude upwelling effect and horizontal transportation. It is also necessary to note that the horizontal transport of O and N_2 is much slower than the vertical acoustic-gravity waves. And therefore, the penetration of air parcels of lower O/N_2 from high-latitude region to low-latitude region takes several hours before recovery. It can be seen that the O/N_2 ratio depletion penetrated to around 20°S during the first storm while during the second storm to around 40°S. This may imply a larger and more effective atmosphere circulation and horizontal transportation process over the SH during the first storm. Unfortunately, since the GUVI observation is limited between 80°N and 60°S, it is not possible to directly measure the O/N_2 ratio in the southern high-latitude region. The high-latitude mass density and composition change will be analyzed in more detail in next sections.

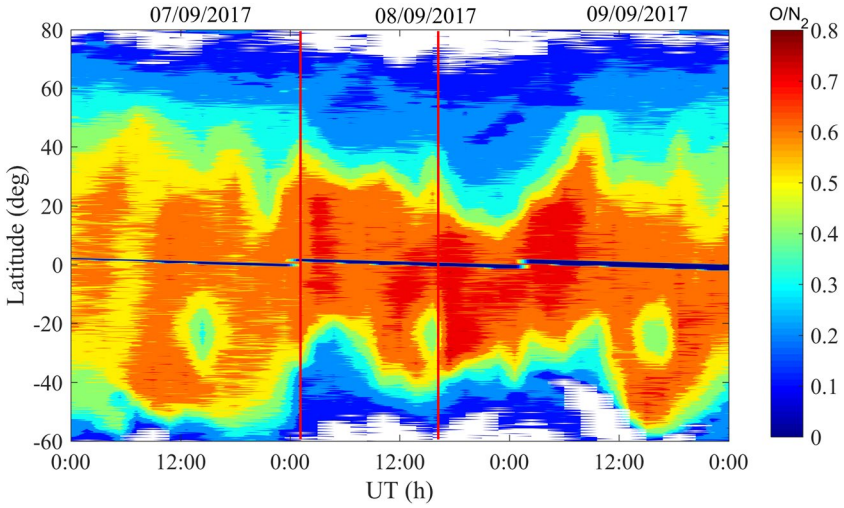

Figure 3. O/N_2 ratio distribution from GUVI from 7–9 September 2017. Two red solid lines represent the two onsets of O/N_2 equatorward penetrations. GUVI, Global Ultraviolet Imager.

3. Simulation Results from Models

In this section, we make use of two atmospheric general circulation models, namely TIEGCM and GITM, to study the thermospheric mass density response in a relatively realistic manner (Richmond et al., 1992; Ridley et al., 2006). The TIEGCM is a global model of the thermosphere-ionosphere system, extending from ~100 km to about 500–800 km altitude (depending on solar activity). In this study we use the latest high-resolution version of the model which has a horizontal resolution of 2.5° × 2.5° in geographic latitude and longitude and a vertical resolution of one-fourth scale height, with a total of 57 constant pressure levels. The model's lower boundary is specified by climatological migrating and nonmigrating tides based on the Global Scale Wave Model (Hagan & Forbes, 2002, 2003). The upper boundary energy and momentum inputs include the solar UV and EUV fluxes, energetic particle precipitation, and polar ionospheric electric fields or convection. The TIEGCM model outputs are recorded every 20 min.

GITM is a three-dimensional spherical code that models the Earth's thermosphere and ionosphere system using a stretched grid in latitude and altitude. One major difference between GITM and other numerical simulations thermosphere codes is the use of an altitude grid instead of a pressure grid. The altitude spacing is done automatically using scale-heights and specifying a lower and upper boundary and the number of grid points (Ridley et al., 2006). The GITM model outputs are recorded every 10 min. Any parameter at a given height can be obtained by interpolation. For the simulation in this section, the ionospheric convection patterns are derived from Weimer model. First principle models with upper boundary inputs like Weimer model developed by Weimer (1996) can be useful in quantitatively studying the large-scale structures of thermospheric mass density though the Joule heating power and the thermospheric mass density may be underestimated especially mainly due to the quick variations of electric fields (Deng & Ridley, 2007). The results of Huang et al. (2012) also showed that Joule heating estimations by using the variable electric fields provided by AMIE data assimilation proposed by Richmond and Kamide (1988) produce about 2.5 times as much heating as an empirical model of high-latitude fields.

Maps of (first row) height-integrated Joule heating, (second row) O/N_2 ratio, (third row) mass density and (fourth row) neutral temperature on September 8, 2017 based on TIEGCM are presented in Figure 4 while similar maps of (first row) height-integrated Joule heating, (second row) mass density percentage deviation, (third row) mass density and (fourth row) neutral temperature based on GITM are given in Figure 5. As is mentioned earlier, in TIEGCM and GITM we usually underestimate the Joule heating and thermospheric mass density. For instance, the maximum value of mass density at 350 km can be as much as 3×10^{-11} kg / m^3 from in situ observations. However, in TIEGCM and GITM, the maximum values are less than 1×10^{-11} kg / m^3 and 2×10^{-11} kg / m^3 at the same altitude, respectively. However, though the

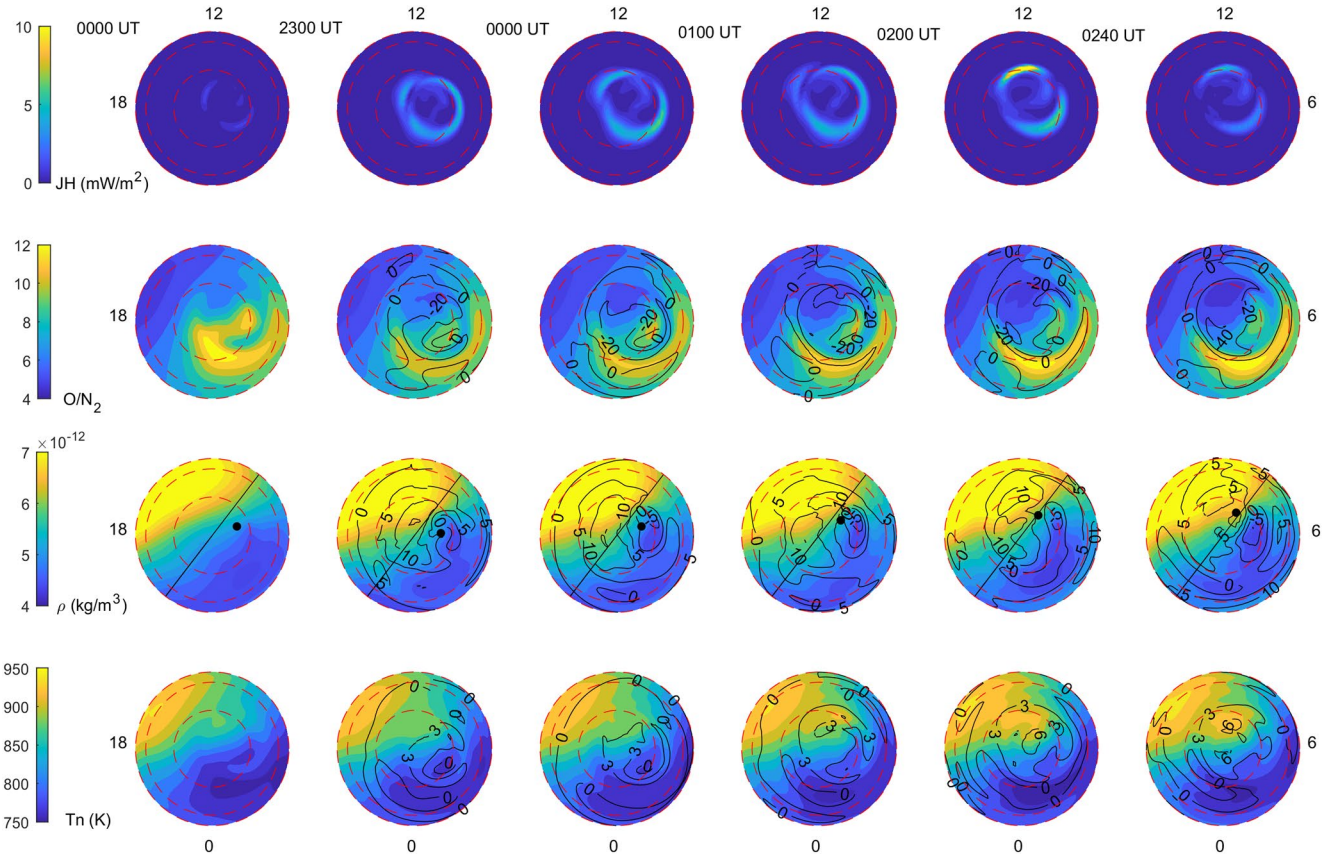

Figure 4. Maps of (first row) height-integrated Joule heating, (second row) O/N_2 ratio, (third row) mass density and (fourth row) neutral temperature on September 8, 2017 from 0000 UT to 0240 UT on September 8, 2017 based on TIEGCM. The contours represent the mass density percentage deviation. The black solid lines indicate the GRACE trajectory along which the LD1 and LD2 was observed. The three dashed circles represent the geographical equator, 30° and 60°, respectively outside in. The black solid dot represents the geomagnetic south pole. GRACE, Gravity Recovery and Climate Experiment; TIEGCM, Thermosphere-Ionosphere Electrodynamic General Circulation Model.

thermospheric mass density can be underestimated with empirical Weimer model, the GITM model reproduces quite well the low-density cells LD1 over the SH during the first storm. The integrated Joule heating power of GITM model in the dawn-side auroral region increases from about 1 mW/m^2 to more than 5 mW/m^2 in 2 h. Around 0130 UT the Joule heating power peaked and then started to decrease. The formation of low-density cells started almost concurrently with the increase of Joule heating at 0000 UT. Referring to Figures 4 and 5, it is evident that the location of main Joule heating area is not coincident with that of density cells (both high-density cell in the noon sector and low-density cell in the dawn sector). Meanwhile, the mass density map in TIEGCM model tends to have a two-cell pattern but the mass density deviation (~10%) inside the cell is much smaller than that in GITM (~50%). In terms of the locations of low-density cells, only the location of LD1 can be reproduced in GITM while in TIEGCM the center of low-density cell locates earlier in local time than that of the LD1 cell. At around 0230 UT, the noon high-density cell starts to fade and the dawn and dusk low-density cells expand and then merge. The UT time (0300 UT) when LD1 was observed is also consistent with that predicted by GITM (~0230 UT). However, neither of the models reproduces LD2 at the same time. Additionally, if we focus on the last column in Figure 5, we can see that the low-density cells can persist and even expand without a high level of Joule heating, which indicates that the local heating and induced thermal expansion is not the direct driving force of the density-cells. The low-density cells are supposed to be controlled by the dynamics of the thermosphere.

The O/N_2 ratio are nearly anticorrelated, but not linearly, with the neutral temperature in Figure 4. This is because the temperature profile directly determines the scale height of each constituents and the O/N_2 ratio is determined by the scale heights of O and N_2 in relatively slow processes that have a time scale of

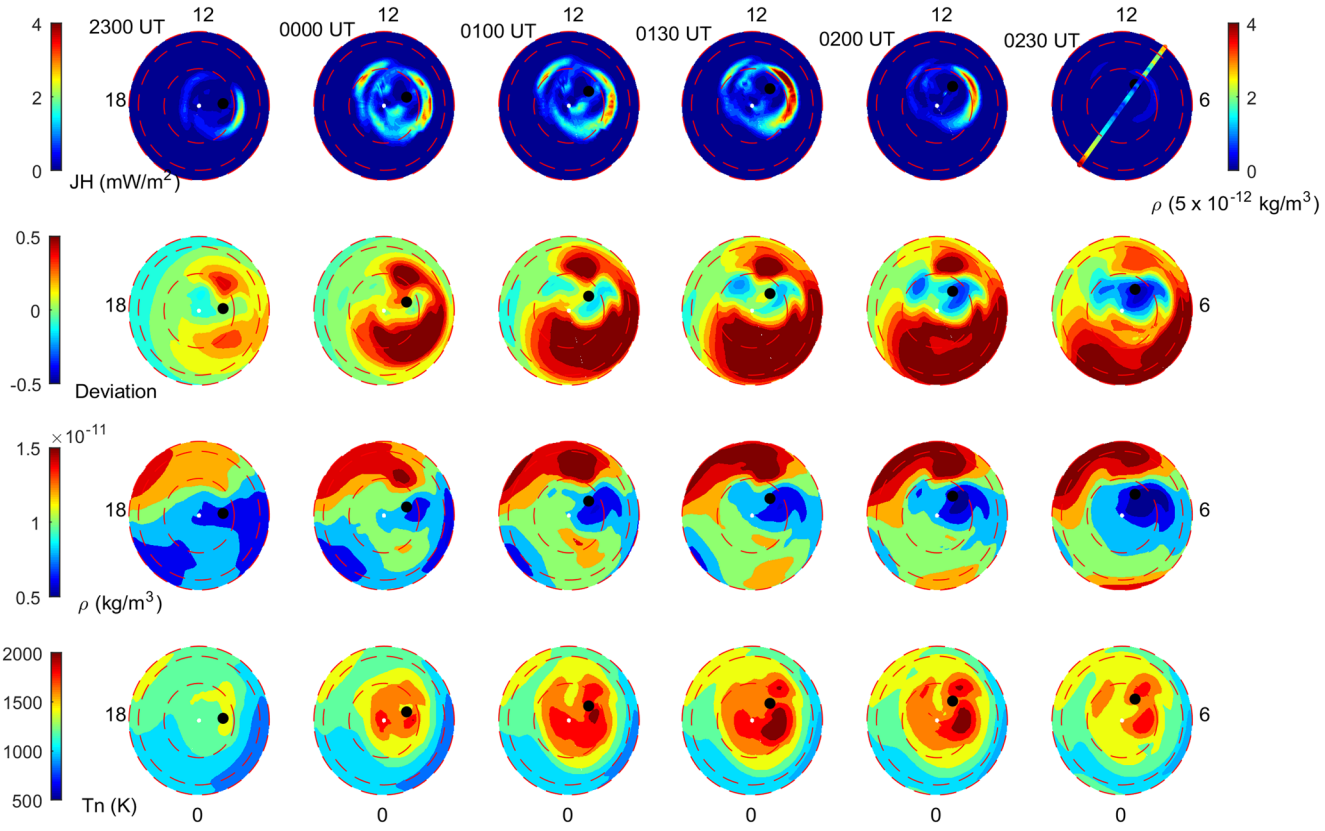

Figure 5. Maps of (first row) height-integrated Joule heating, (second row) mass density percentage deviation, (third row) mass density and (fourth row) neutral temperature from 2300 UT on 7 September to 0230 UT on September 8, 2017 based on GITM. The small colored dots in the last column indicate the GRACE trajectory along which the LD1 and LD2 was observed, with the color of each dot corresponding to the mass density value measured by GRACE. The three dashed circles represent the geographical equator, 30° and 60°, respectively outside in. The black solid dot represents the geomagnetic south pole. GITM, Global Ionosphere Thermosphere Model; GRACE, Gravity Recovery and Climate Experiment.

hours. During the second storm low-density cell LD3 cannot be reproduced in both models with the Weimer electric potential inputs. The ion convection in the polar region is mainly controlled by the IMF and modulated by the ionospheric conductivity. The commonly used empirical electric potential model merely includes the rotation effect and interhemispheric asymmetry of IMF B_Y on the electrostatic potential. The deviation of the simulated conductivity from the actual conductivity in the numerical simulation may break the mirror symmetry from dusk to dawn and also modulate the location of the center of the cell structure (Tanaka, 2001). Besides, the accumulative discrepancy between simulation and reality can become larger and larger with time.

4. Discussion

4.1. The Effect of IMF B_Y

A numerical simulation is designed for elucidating the effect of IMF on the electric potential and neutral mass density variations in the high-latitude region at the upper thermosphere. In this work, the Weimer electric potential model is used for deriving the high-latitude electric field of GITM. The solar radio flux index F10.7 is set to 80 sfu to represent the equinox solar minimum condition. The solar wind speed is set to 600 km/s and the plasma density is set to 60 n/cc. The IMF B_X and B_Z are set to 0 and 5, respectively, which represents a slightly northward condition. These settings are applied for both simulations, which will be described in detail below. In order to investigate the effect of the IMF BY component on the composition, the simulations were repeated with B_Y values of +10 and −10 nT. Each simulation was run to a

diurnally reproducible state with the cross-cap potential held constant for 5 days. IMF By effects on the electric potential pattern can be contrary for different hemisphere. The cross polar cap potential increases from 60 to 100 kV over the south polar region while over the north polar region it decreases from 100 to 60 kV. Despite the potential changes, the flow across the polar region is rotated counterclockwise over the south polar region and clockwise over the north polar region. Ion flows from regions with high potentials to those with low potentials. The induced horizontal winds give rise to a cell of lower (higher) pressure that locates near the high-potential (low-potential) cell in a quasisteady state. In the last row in Figure 6, the location of density depletion is consistent with the location of potential rise. It is understood that between two quasisteady states, the ion drags rather than the background temperature-driven winds induce the additional divergent flow. The speed of divergent neutral flow away from the cell center mainly depends on electric fields and ion-neutral collision frequency. We note that the electron-neutral collisions are insignificant since the electron-neutral collision frequency multiplied by the electron mass is much smaller than the ion-neutral collision frequency multiplied by the ion mass. When B_Y is −10 nT, no density cell structure can be seen in neither north polar region nor south polar region. But when B_Y becomes +10 nT, an isolated dawn-side low-density cell is generated over the south polar region. The local time of this low-density cell is similar to that of cells in Figure 4. However, the three low-density cells over the SH were observed under B_Y negative condition, which is shown not to be beneficial to the formation of density cells. This indicates that some other processes may facilitate the formation of the density cells. If we compare density patterns over two hemispheres, it seems that cell structures are easier to be generated over the SH than over the NH at 0200 UT. This may be explained by the geometry of the ion convection. The high-potential cell locates at midnight (dawn) in the north (south) polar region. The background wind in the polar region is more dominant at midnight than at dawn. And therefore, we do not see any wind reversal over the NH, which can be regarded as an indicator of cyclone or anticyclone. This might explain why no cell structure over the NH was observed by GRACE at the similar time when LD1 was observed.

4.2. The Effect of Vertical Wind

In the explanations of Schoendorf et al. (1996), the horizontal winds driven by ion drags are the only cause of the cyclonic (or anticyclonic) structure, which is the supposed reason for the low-density cell (or high-density cell). Since the hydrostatic equilibrium is assumed throughout TIEGCM, the vertical wind velocities are generally much smaller than the horizontal wind velocities in TIEGCM. However, the hydrostatic equilibrium is not valid for short-period (less than minutes) motions and the atmospheric circulation that consists of both vertical and horizontal motions proves to be important in the storm-time thermosphere. As is described by Ridley et al. (2006), one of the main differences between TIEGCM and GITM is the completely solved vertical momentum equation incorporated in GITM. The vertical momentum equation can be written in the earth-fixed spherical coordinate as

$$\frac{\partial u_r}{\partial t}+u_r\frac{\partial u_r}{\partial r}+u_\theta\frac{\partial u_r}{r\partial\theta}+u_\phi\frac{\partial u_r}{r\cos(\theta)\partial\phi}+\frac{k}{M}\frac{\partial T}{\partial r}+\frac{kT}{M}\frac{\partial N}{\partial r}=g+F+\frac{u_\theta^2+u_\phi^2}{r}+\cos^2(\theta)\Omega^2 r+2\cos(\theta)\Omega u_\phi \quad (3)$$

where u_r is the vertical neutral wind velocity, u_θ is the northward neutral wind velocity, u_ϕ is the eastward neutral wind velocity, M is the molecular mass, T is the neutral temperature, g is the earth gravity, and F is the friction term. In order to investigate the effects of vertical winds derived from different vertical momentum equations, we present the minimal density deviation in the high latitude regions based on GITM and TIEGCM simulations in Figure 7. The minimal density deviation is simply the minimum of the all density deviations in the high latitude regions. By comparing the simulated mass density deviations in TIEGCM and GITM, the minimal mass density deviation in GITM simulations is approximately −50% while that in TIEGCM is −20%. Referring to Figures 2 and 7, the minimal density deviation in GITM is similar to that of LD1 observed by GRACE (−50%). Besides, if we focus on the period before and after this geomagnetic storm, that is on seventh and ninth, the low-density cell structure still exists in GITM instead of TIEGCM. But the minimal density deviation is lower (−20%) after the geomagnetic storm than that during storm time.

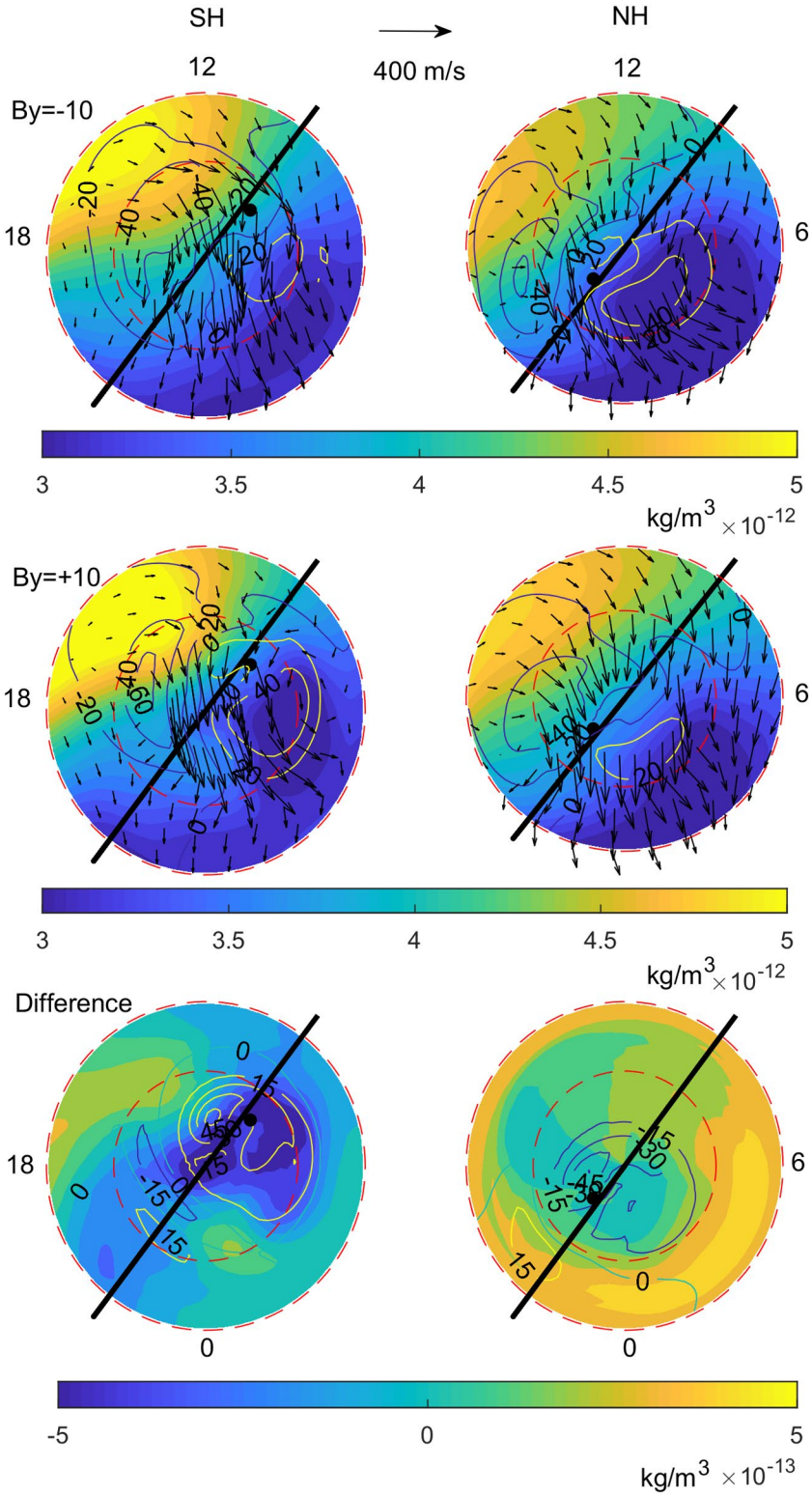

Figure 6. Maps of total mass density and electric potential distributions based on diurnally reproducible TIEGCM runs in case of negative B_Y (first row) and positive B_Y (second row). The bottom panel shows the difference between the two B_Y conditions. The contours represent the electric equipotential lines with unit kV. All maps are plotted at 0200 UT. The outer circles represent 30° latitude. TIEGCM, Thermosphere-Ionosphere Electrodynamic General Circulation Model.

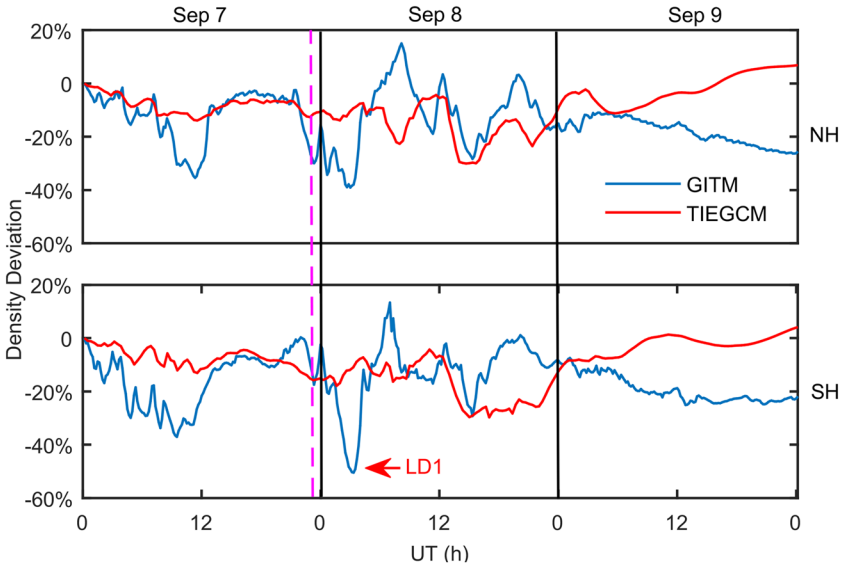

Figure 7. The minimal density deviation in the high latitude region of the NH (upper panel) and SH (lower panel) based on GITM (blue) and TIEGCM (red) simulations. The purple line represents the sudden storm commencement at around 2302 UT on September 7, 2017. GITM, Global Ionosphere Thermosphere Model; TIEGCM, Thermosphere-Ionosphere Electrodynamic General Circulation Model.

Figure 8 shows different terms in continuity equations incorporated in GITM. As is seen, the horizontal velocity divergence term (first column) is predominant at 0000 UT and 0100 UT in the formation of low-density cells while the vertical advection term (fourth column) dominates other terms at 0200 UT. It indicates that the horizontal velocity divergence term can be the main cause of low-density cells at first and then decrease gradually and with the development of low-density cells the vertical advection term becomes more and more important. The winds may be driven by two processes, one of which is the local heating in the higher altitude or particle precipitation. The local heating process increases the vertical temperature gradient and then drives vertical winds. The other process is the horizontal transport. The horizontal transport can lead to a mass accumulation or loss that may be divided into two parts: (1) the change of number density and (2) the change of mean molecular mass. It is important to note that the role of horizontal transport here is not similar to the role of horizontal winds that cause the cyclonic structure. Even if the horizontal wind is divergent free it can still lead to a change of number density or mean molecular mass simultaneously provided the horizontal gradient of pressure scale height is not completely eliminated.

Referring to Figure 1 there was a simultaneous boost in solar wind plasma temperature and speed which is shown by the black dashed line at around 0130 UT on 8 September. In the third row of Figure 8 we can see the increase in vertical divergence term that results from the particle precipitation at 0130 UT on 8 September. The particle precipitation significantly increases the ionospheric conductivities and enhances Joule heating power, which can be seen in the fourth column of Figure 5. The vertical wind perturbations along dawn-dusk meridian are shown in Figure 9 as an example. Significant depletions in vertical winds along the dawn-dusk meridian at 350 km occur at 0130 UT. Referring to Equation 3, this indicates that the particle precipitations may drive a large downwards wind via the term F containing ion-neutral and neutral-neutral collision (Colegrove et al., 1966; Rees, 1989). The strengths of wind perturbations along the dawn-dusk meridian are highly anisotropic in local time. The amplitudes of wind perturbations can be more than two times larger at dawn than at dusk, which is similar to the distribution of height-integrated Joule heating in Figure 5. In GITM the speed of vertical wind can be a magnitude of 100 m/s at the upper thermosphere. The period of vertical wind perturbation is ~17 min, which is consistent with the typical period of gravity waves at this altitude. As the existence of large vertical winds enhances the circulation in the adjacent area, the locations of density cells are modulated and not perfectly coincident with the area of divergent horizontal flows.

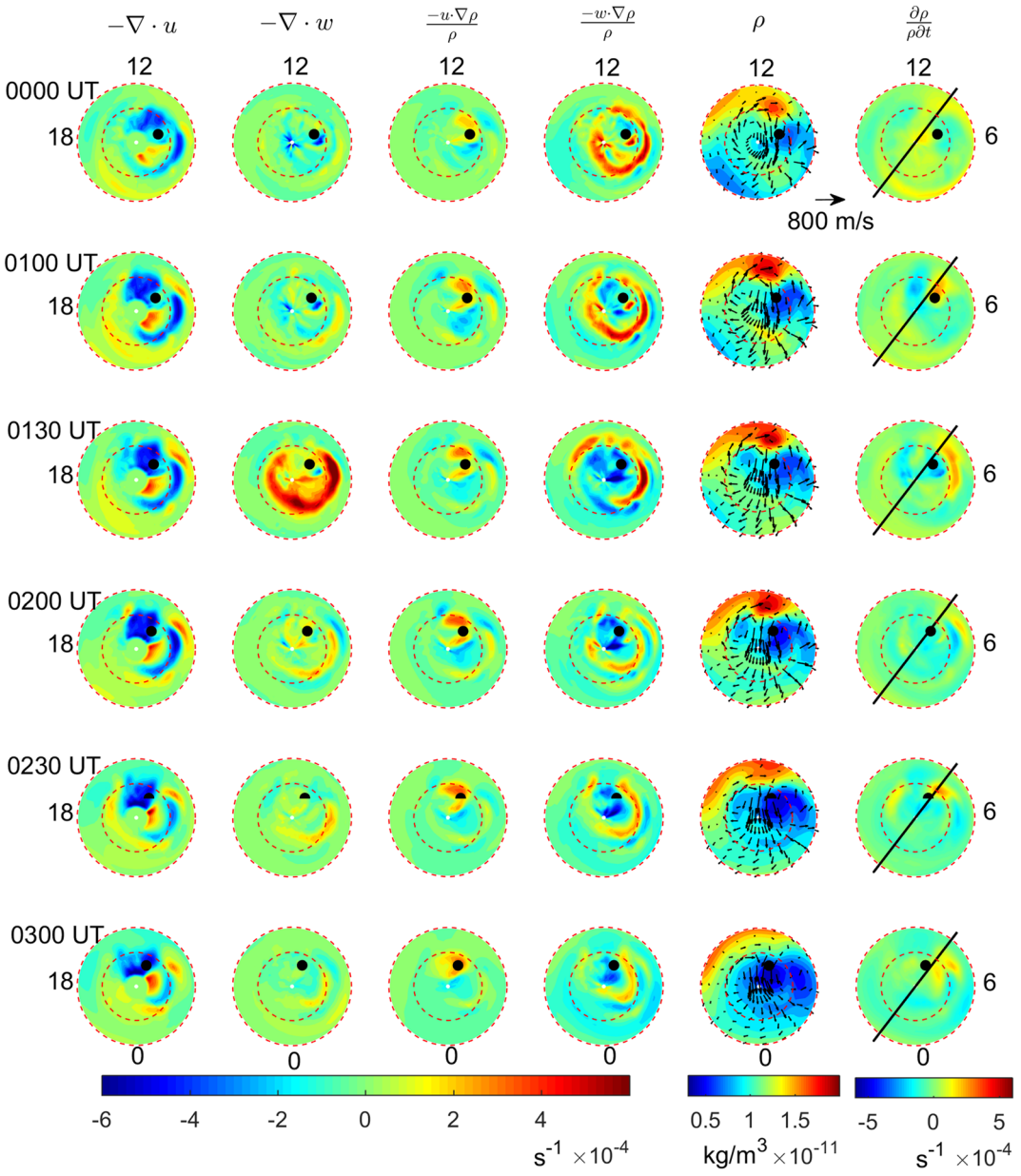

Figure 8. Terms in continuity equations in the GITM simulations over the SH. The two dashed circles represent the 30° and 60°, respectively outside in. The black solid dot represents the geomagnetic south pole. GITM, Global Ionosphere Thermosphere Model.

5. Conclusions

Evidences of the existence of low-density cells at the height of 350 km are reported based on GRACE in situ observations during the September 2017 geomagnetic storm. The possible formation mechanism of low-density cells is studied with the help of numerical simulation models TIEGCM and GITM. The main conclusions in this study are as follows:

1. According to GRACE observations and corresponding GITM simulation, the critical height of observable low-density cells is confirmed to be not less than 350 km, or more precisely between 350 and 450 km under solar minimum condition, which is not consistent with the theoretical conclusion based on TIEGCM. The latitudinally spatial scale of observed low-density cells at 350 km are 1,500–2,000 km, which is comparable with the predicted scales based on TIEGCM

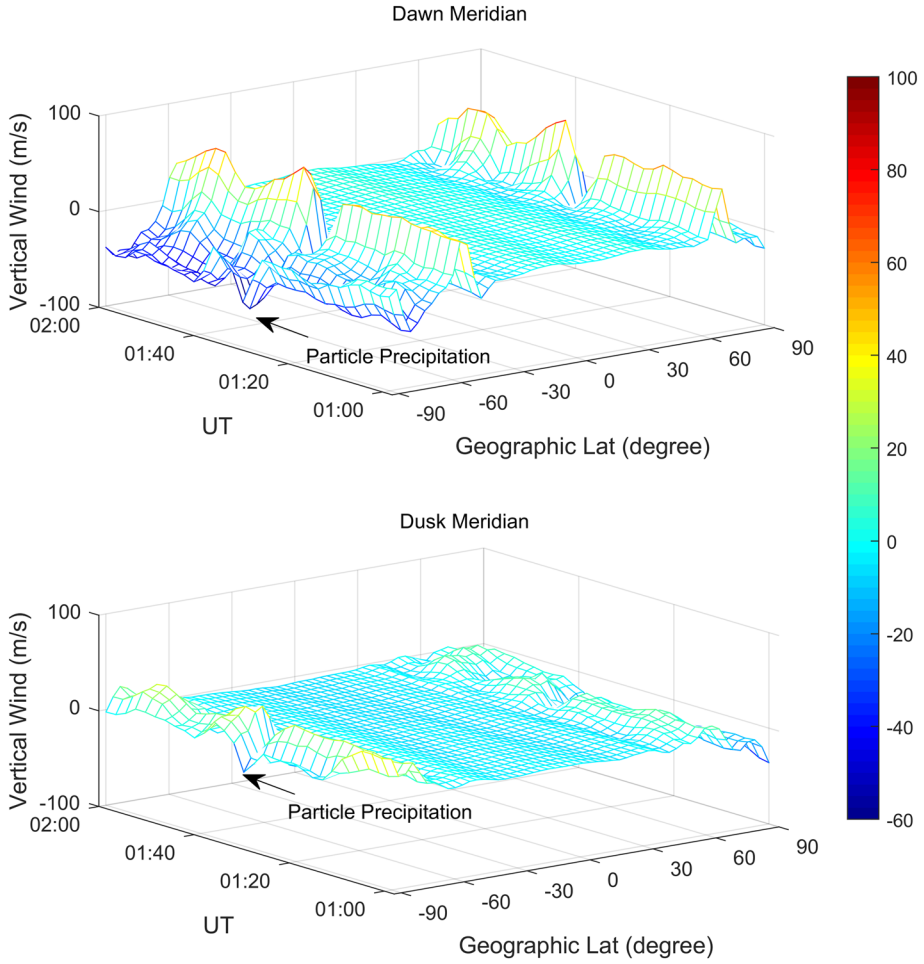

Figure 9. Vertical wind perturbations along the dawn-dusk meridian at an altitude of 350 km in GITM from 0100 UT to 0200 UT on 8 September. GITM, Global Ionosphere Thermosphere Model.

2. The TIEGCM and GITM simulations driven by empirical convection models are unable to reproduce the morphology of the low-density cells observed by GRACE at 350 km except that GITM captures the general features of the earliest low-density cell (LD1). The underestimation of energy inputs can be the most important reason why TIEGCM fails to reproduce the LD1. Techniques with higher time resolutions like AMIE are needed to explain the discrepancy between observations and numerical simulations
3. Three low-density cells, including two in the dawn sector and one in the night sector were observed just before the direction of IMF B_Y turned from negative to positive. The numerical simulations based on TIEGCM shows that both the minimal mass density inside the low-density cell and the size of the low-density cell may be related to the directions of IMF B_Y component. The positive (negative) IMF B_Y leads to larger cross polar cap potential over the south (north) polar region. Larger cross polar cap electric fields give rise to a better-organized density cell pattern in the high-latitude region
4. The effect of vertical winds can be comparable with that of horizontal winds when energetic particles are injected into the auroral region. Gravity waves are generated by local heating from lower atmosphere propagating upwards and give rise to the contemporary vertical wind variation. The speed of vertical wind can be a magnitude of 100 m/s at the upper thermosphere. The large vertical wind enhances the circulation in the adjacent area and modulates the density cell patterns as well

Both the GRACE observation and numerical simulation indicate that the low-density cell structure is the inherent nature of the thermosphere in geomagnetic active periods. During strong geomagnetic storms, the deviation from the quiet-time average density can be up to 60% at an altitude of 350 km. The inclusion of

low-density cell structures in the empirical thermospheric density model is crucial for the improvement of model accuracies, especially in the high latitude regions.

Data Availability Statement

GRACE data are available through Yuan et al. (2019). Simulation results have been provided by the Community Coordinated Modeling Center at Goddard Space Flight Center through their public Runs on Request system (http://ccmc.gsfc.nasa.gov). The TIEGCM Model was developed by the R. G. Roble et al. at the National Center for Atmospheric Research. The GITM Model was developed by the A. J. Ridley et al. at the University of Michigan.

Acknowledgment
This work was supported by the National Natural Science Foundation of China-German Science Foundation (NSFC-DFG) Project (Grant No. 41761134092), National Natural Science Foundation of China (NSFC) Project (Grant No. 12073012), Jiangsu Province Distinguished Professor Project (Grant No. R2018T20) and Shanghai Leading Talent Project (Grant No. E056061). Authors thanked the teams for providing GRACE acceleration, O/N_2 as well as space weather indices. Authors also thanked the Community Coordinated Modeling Center and model developers for running the TIEGCM and GITM models.

References

Araki, T. (1994). A physical model of the geomagnetic sudden commencement. In M. Engebretson, K. Takahashi, & M. Scholer (Eds.), *Solar wind sources of magnetospheric ultra-low frequency waves Geophysics Monograph Series 81* (pp. 183–200). Washington, DC: AGU.

Aruliah, A. L., Griffin, E. M., Aylward, A. D., Ford, E. A. K., Kosch, M. J., Davis, C. J., et al. (2005). First direct evidence of meso-scale variability on ion-neutral dynamics using co-located tristatic FPIs and EISCAT radar in Northern Scandinavia. *Annales Geophysicae*, *23*(1), 147–162. https://doi.org/10.5194/angeo-23-147-2005

Bruinsma, S., Forbes, J. M., Nerem, R. S., & Zhang, X. (2006). Thermosphere density response to the 20–21 November 2003 solar and geomagnetic storm from CHAMP and GRACE accelerometer data. *Journal of Geophysical Research*, *111*(A6). https://doi.org/10.1029/2005ja011284

Bruinsma, S., Tamagnan, D., & Biancale, R. (2004). Atmospheric densities derived from CHAMP/STAR accelerometer observations. *Planetary and Space Science*, *52*, 297–312. https://doi.org/10.1016/j.pss.2003.11.004

Calabia, A., & Jin, S. (2016). Thermospheric mass density variations during the March 2015 geomagnetic storm from GRACE accelerometers. In *2016 Progress in Electromagnetic Research Symposium (PIERS), August 8-11, 2016, Shanghai, China*. (pp. 4976–4980). IEEE. Retrieved from https://ieeexplore.ieee.org/abstract/document/7735812

Calabia, A., & Jin, S. G. (2017). Thermospheric density estimation and responses to the March 2013 geomagnetic storm from GRACE GPS-determined precise orbits. *Journal of Atmospheric and Solar-Terrestrial Physics*, *154*, 167–179. https://doi.org/10.1016/j.jastp.2016.12.011

Colegrove, F., Johnson, F., & Hanson, W. (1966). Atmospheric composition in the lower thermosphere. *Journal of Geophysical Research*, *71*, 2227.

Crowley, G., Emery, B. A., Roble, R. G., Carlson, H. C., & Knipp, D. J. (1989). Thermospheric dynamics during September 18–19, 1984: 1. Model simulations. *Journal of Geophysical Research*, *94*(A12), 16925–16944. https://doi.org/10.1029/JA094IA12P16925

Crowley, G., Immel, T. J., Hackert, C. L., Craven, J., & Roble, R. G. (2006). Effect of IMF BY on thermospheric composition at high and middle latitudes: 1. Numerical experiments. *Journal of Geophysical Research*, *111*, A10311. https://doi.org/10.1029/2005JA011371

Crowley, G., Schoendorf, J., Roble, R. G., & Marcos, F. A. (1996). Cellular structures in the high-latitude thermosphere. *Journal of Geophysical Research*, *101*(A1), 211–223. https://doi.org/10.1029/95JA02584

Deng, Y., & Ridley, A. J. (2007). Possible reasons for underestimating Joule heating in global models: E field variability, spatial resolution, and vertical velocity. *Journal of Geophysical Research*, *112*, A09308. https://doi.org/10.1029/2006JA012006

Doornbos, E., Bruinsma, S., Fritsche, S., Koppenwallner, G., Visser, P., van den IJssel, J., & de Teixeira de Encarnacao, J. (2014). *TU GOCE+ theme 3: Air density and wind retrieval using GOCE data*. Final report Technical Report 4000102847/NL/EL. Delft, Netherlands: Eodisp.

Forbes, J. M., Gonzalez, R., Marcos, F. A., Revelle, D., & Parish, H. (1996). Magnetic storm response of lower thermospheric density. *Journal of Geophysical Research*, *101*(A2), 2313–2319. https://doi.org/10.1029/95ja02721

Guo, D., Lei, J., Ridley, A., & Ren, D. (2019). Low-density cell of the thermosphere at high latitudes revisited. *Journal of Geophysical Research: Space Physics*, *124*, 521–533. https://doi.org/10.1029/2018JA025770

Hagan, M. E., & Forbes, J. M. (2002). Migrating and nonmigrating diurnal tides in the middle and upper atmosphere excited by tropospheric latent heat release. *Journal of Geophysical Research*, *107*(D24), 4754. https://doi.org/10.1029/2001JD001236

Hagan, M. E., & Forbes, J. M. (2003). Migrating and nonmigrating semidiurnal tides in the upper atmosphere excited by tropospheric latent heat release. *Journal of Geophysical Research*, *108*(A2), 1062. https://doi.org/10.1029/2002JA009466

Huang, Y., Deng, Y., Lei, J., Ridley, A., Lopez, R., Allen, R. C., & Butler, B. M. (2012). Comparison of Joule heating associated with high-speed solar wind between different models and observations. *Journal of Atmospheric and Solar-Terrestrial Physics*, *75–76*, 5–14.

Innis, J. L., & Conde, M. (2002). Characterization of acoustic–gravity waves in the upper thermosphere using Dynamics Explorer 2 Wind and Temperature Spectrometer (WATS) and Neutral Atmosphere Composition Spectrometer (NACS) data. *Journal of Geophysical Research*, *107*(A12), 1418. https://doi.org/10.1029/2002JA009370

Jin, S. G., Calabia, A., & Yuan, L. L. (2018). Thermospheric variations from GNSS and accelerometer measurements on small satellites. *Proceedings of the IEEE*, *106*(3), 484–495. https://doi.org/10.1109/JPROC.2018.2796084

Liu, H., & Lühr, H. (2005). Strong disturbance of the upper thermospheric density due to magnetic storms: CHAMP observations. *Journal of Geophysical Research*, *110*, A09S29. https://doi.org/10.1029/2004JA010908

Meier, R., Crowley, G., Strickland, D., Christensen, A., Paxton, L., Morrison, D., & Hackert, C. (2005). First look at the 20 November 2003 superstorm with TIMED/GUVI: Comparisons with a thermospheric global circulation model. *Journal of Geophysical Research*, *110*(A9). https://doi.org/10.1029/2004ja010990

Rees, D. (1989). *Physics and chemistry of the upper atmosphere*. New York, NY: Cambridge University Press.

Richmond, A. D., & Kamide, Y. (1988). Mapping electrodynamic features of the high-latitude ionosphere from localized observations: Technique. *Journal of Geophysical Research*, *93*, 5741–5759.

Richmond, A. D., Ridley, E. C., & Roble, R. G. (1992). A thermosphere/ionosphere general circulation model with coupled electrodynamics. *Geophysical Research Letters*, *19*(6), 601–604. https://doi.org/10.1029/92GL00401

Ridley, A., Deng, Y., & Toth, G. (2006). The global ionosphere-thermosphere model. *Journal of Atmospheric and Solar-Terrestrial Physics*, *68*(8), 839–864. https://doi.org/10.1016/J.JASTP.2006.01.008

Schoendorf, J., & Crowley, G. (1995). Interpretation of an unusual high latitude density decrease in terms of thermospheric density cells. *Geophysical Research Letters*, *22*(22), 3023–3026. https://doi.org/10.1029/95GL02226

Schoendorf, J., Crowley, G., & Roble, R. (1996). Neutral density cells in the high latitude thermosphere-2. Mechanisms. *Journal of Atmospheric and Terrestrial Physics*, *58*(15), 1769–1781.

Smith, R. W., & Hernandez, G. (1995). Vertical winds in the thermosphere within the polar cap. *Journal of Atmospheric and Terrestrial Physics*, *57*, 611–620.

Strickland, D., Evans, J., & Paxton, L. (1995). Satellite remote sensing of thermospheric O/N2 and solar EUV: 1. *Journal of Geophysical Research*, *100*, 12217–12226.

Sutton, E. K., Forbes, J. M., & Nerem, R. S. (2005). Global thermospheric neutral density and wind response to the severe 2003 geomagnetic storms from CHAMP accelerometer data. *Journal of Geophysical Research*, *110*, A09S40. https://doi.org/10.1029/2004JA010985

Tanaka, T. (2001). Interplanetary magnetic field By and auroral conductance effects on high-latitude ionospheric convection patterns. *Journal of Geophysical Research*, *106*(A11), 24505–24516. https://doi.org/10.1029/2001JA900061

Thayer, J. P., Liu, X., Lei, J., Pilinski, M., & Burns, A. G. (2012). The impact of helium on thermosphere mass density response to geomagnetic activity during the recent solar minimum. *Journal of Geophysical Research*, *117*, A07315. https://doi.org/10.1029/2012JA017832

Weimer, D. R. (1996). A flexible, IMF dependent model of high-latitude electric potential having "space weather" applications. *Geophysical Research Letters*, *23*, 2549.

Yamazaki, Y., Kosch, M. J., & Sutton, E. K. (2015). North-south asymmetry of the high-latitude thermospheric density: IMF BY effect. *Geophysical Research Letters*, *42*, 225–232.

Yuan, L. L., Jin, S. G., & Calabia, A. (2019). Distinct thermospheric mass density variations following the September 2017 geomagnetic storm from GRACE and Swarm. *Journal of Atmospheric and Solar-Terrestrial Physics*, *184*, 30–36. https://doi.org/10.1016/j.jastp.2019.01.007